Focused ion beam micromachining of eukaryotic cells for cryoelectron tomography

Alexander Rigort[1], Felix J. B. Bäuerlein[1], Elizabeth Villa, Matthias Eibauer, Tim Laugks, Wolfgang Baumeister[2], and Jürgen M. Plitzko[2]

Department of Molecular Structural Biology, Max Planck Institute of Biochemistry, Am Klopferspitz 18, D-82152 Martinsried, Germany

Contributed by Wolfgang Baumeister, January 24, 2012 (sent for review November 21, 2011)

Cryoelectron tomography provides unprecedented insights into the macromolecular and supramolecular organization of cells in a close-to-living state. However because of the limited thickness range (< 0.5–1 μm) that is accessible with today's intermediate voltage electron microscopes only small prokaryotic cells or peripheral regions of eukaryotic cells can be examined directly. Key to overcoming this limitation is the ability to prepare sufficiently thin samples. Cryosectioning can be used to prepare thin enough sections but suffers from severe artefacts, such as substantial compression. Here we describe a procedure, based upon focused ion beam (FIB) milling for the preparation of thin (200–500 nm) lamellae from vitrified cells grown on electron microscopy (EM) grids. The self-supporting lamellae are apparently free of distortions or other artefacts and open up large windows into the cell's interior allowing tomographic studies to be performed on any chosen part of the cell. We illustrate the quality of sample preservation with a structure of the nuclear pore complex obtained from a single tomogram.

cryoTEM lamella | frozen-hydrated cells | cryoFIB | subtomogram averaging | electron-transparent windows

Electron tomography (ET) of frozen-hydrated biological materials (cryoET) provides three-dimensional (3D) images without compromising on structural preservation (1, 2). However, only sufficiently small objects (< 500 nm) can be examined in toto by cryoET and with a resolution that is high enough for the detection and identification of molecular structures using pattern recognition methods (3). Therefore, the application of cryoET has been restricted to viruses, small prokaryotic cells, isolated organelles or suitably thin peripheral regions, appendages, and protrusions of eukaryotic cells (4–7). The bulk volume of most eukaryotic cells exceeds the thickness accessible by today's intermediate voltage transmission electron microscopes (TEMs) and even high voltage instruments (> 1, 000 kV) would not expand the accessible thickness range sufficiently.

For studying eukaryotic cells at molecular resolution it is necessary to develop tools and techniques providing controlled access to structural features buried deep inside cellular volumes. Many supramolecular structures of great interest, such as centrosomes, or kinetochores are present only in low copy numbers or are so deeply rooted in their cellular environments that it is not possible to isolate them without violating their structural integrity. Hence, it is highly desirable to study them in situ, and, indeed, the concept of doing structural biology in situ is an appealing one. Literally, this concept requires to open up 'windows' into the cell's interior.

Cryoultramicrotomy (8–10) is currently the method of choice for producing thin (50–200 nm) frozen-hydrated sections of cells and tissues. In spite of considerable efforts to develop cryosectioning into a routine technique, it remains a challenge to its practitioners to prepare such sections and to deposit them on EM grids with good thermal and electrical contact. But the main problem with cryosectioning is a massive (> 30%) compression of the sections and the concomitant distortions of cellular structures. There is no remedy so far for this problem.

An alternative approach avoiding mechanical compressions is the use of focused ion beam (FIB) technology, where thinning of the frozen-hydrated specimen is achieved through the process of sputtering with gallium ions. Pilot studies have shown that cryoFIB milling can indeed be applied to frozen-hydrated material, rendering cellular samples transparent enough for TEM (11–13). However, the simple ablation geometries used in these studies would not permit to address structures embedded deeply in cellular volumes in a targeted manner. Approaches such as used in the materials science (see e.g., ref. 14), namely to prepare thin electron transparent windows, lift them out, and place them on EM grids, are difficult if not impossible to realize with samples which must be kept below the devitrification temperature (< −140 °C) at all times.

Here we describe a unique FIB-based approach for the preparation of cellular samples which fulfill all the requirements of cryoET and which is applicable to all kinds of cells grown or deposited directly on EM grids. With the ion beam incident under a shallow angle, material is removed from above and below the target structures. This approach leaves behind a thin (< 500 nm) lamella supported on both sides by the bulk ice. Because the whole procedure is carried out on the EM grid, transfer to the TEM cryoholder and into the TEM is a routine operation. The milled lamellae open up large windows into the interior of the cells devoid of artefacts.

Results

Preparation of Frozen-Hydrated Cells for Cryoelectron Microscopy. Our experimental approach is based on the use of FIB technology for the micromachining of cells embedded in vitreous ice. Thin lamellae are cut out of cellular volumes with geometries suitable for electron tomography. The lamellae are left in situ during transfer to the EM supported only by the surrounding bulk ice. A scheme of the workflow and our preferred milling geometry are shown in Fig. 1 *A–D*.

Dictyostelium discoideum cells were grown on holy carbon-coated gold grids and subjected to plunge freezing. To facilitate the otherwise delicate handling of the gold grids covered with the thin and fragile ice layer, the grids were mounted on a rigid frame ('autogrid') modified such that the rim did not obstruct the ion beam when incident under shallow angles (Fig. 1*B*; Fig. S1). A target cell or a specific region of it were selected by operating the dual beam instrument in the scanning electron microscopy (SEM) mode. Then a rectangular sector below and above the selected volume were exposed to the gallium beam leaving behind a

Author contributions: A.R. and F.J.B.B. performed cryoFIB work; A.R. performed cryoET; A.R., E.V., and M.E. analyzed data; T.L. realized engineering; A.R., E.V., W.B., and J.M.P. designed research and wrote the paper.

The authors declare no conflict of interest.

Freely available online through the PNAS open access option.

[1]A.R. and F.J.B.B. contributed equally to this work.

[2]To whom correspondence may be addressed. E-mail: baumeist@biochem.mpg.de or plitzko@biochem.mpg.de.

This article contains supporting information online at www.pnas.org/lookup/suppl/doi:10.1073/pnas.1201333109/-/DCSupplemental.

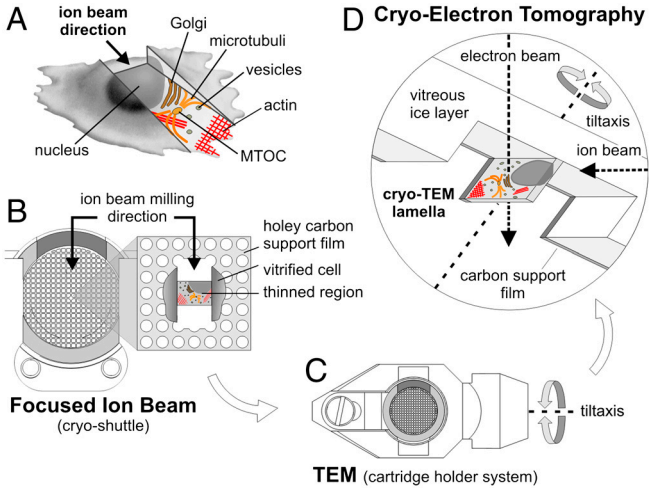

Fig. 1. Schematic of the in situ TEM lamella preparation method. (*A*) Cartoon illustrating the result of thinning an adherent eukaryotic cell by means of milling with a focused ion beam microscope. The resulting thinned region represents a cutout view of the cytoplasm and is used for subsequent imaging by cryoelectron tomography. MTOC: microtubule-organizing center. (*B*) TEM lamella preparation on an EM grid in the FIB instrument. The EM grid is mounted into a ring-like autogrid framing (light gray), which is modified on one side by a cutout (dark gray) to permit milling from grazing angles (see Fig. S1*B*). The autogrid remains clamped in a cryoholder [cryoshuttle, (12)], which can be shuttered during transfers. A central mesh on the EM grid is selected and milling is performed under grazing angles by applying two milling patterns: One is located above the intended lamella region the second one below that region (compare Fig. 2*A*). (*C*) The autogrid, containing the in situ lamella, is transferred into a TEM holder system with respect to the required tilt axis geometry. (*D*) Schematic perspective cross-section drawing showing imaging of the lamella in the TEM instrument. The in situ lamella is prepared by removing vitreously frozen ice and cellular material as well as the carbon support film with two milling patterns (upper and lower pattern). The resulting lamella region allows tomographic imaging over the full tilt range of the TEM goniometer. Diameter of the autogrid shown: 3.5 mm.

thin lamella supported on both sides by the remaining bulk ice, as described in detail in *Methods*. Typical angles of incidence for the gallium beam were 75° to 85° from the grid surface normal. FIB milling can be performed on multiple regions of interest (usually up to 10 for one grid) before transfer to the TEM. The 200 to 400 nm thick lamellae were found to be stable enough for all subsequent manipulation steps when using the reinforcing autogrids. The lamellae were also stable enough during exposure to the electron beam and we did not observe any indications of devitrification (Fig. S2).

Fig. 2 shows SEM (Fig. 2 *A*–*C*) and TEM (Fig. 2 *D* and *E*) images of a lamella prepared from a *D. discoideum* cell. The window made accessible for TEM covers an area of approximately 25 μm^2 and has a thickness of 300 nm. The projection image (Fig. 2*D*) recorded under low-dose conditions shows a cytoplasmic region with numerous organelles suspended in it. In the tomographic reconstruction (Fig. 2*E*) of the area framed in Fig. 2*D* one can clearly discern microtubules (arrows), interconnected ducts and cisternae as well as ribosomes. Vesicular structures show up spherical, as one would expect them to do in the absence of compression forces.

Cryoelectron Microscopy of Large FIB-Milled Windows. For the exploration of large cellular landscapes it is important to be able to prepare windows of even thickness spanning several micrometers. This approach is demonstrated in Fig. 3 where an area of more than 30 μm^2 is made accessible for TEM investigations. Fig. 3*A* shows extensive parts of the cytoplasm and nucleoplasm of a *D. discoideum* cell. While the cytosol harbors numerous organelles (mitochondria, rough endoplasmic reticulum, vesicular, and tubular components of the vacuolar and endosomal systems) interspersed with myriads of macromolecular complexes, the nucleoplasm appears remarkably homogenous with little indications of spatial variations in density. In the nuclear envelope nuclear pore complexes (NPCs) are visible even at low magnification. All cellular structures appear well preserved with no evidence of damage caused by sample preparation. There is some frost contamination in form of small opaque ice crystals (asterisks in Fig. 3*A*), but this is a minor problem and further improvements in shielding during transfer of the samples to the EM should eliminate it altogether.

For tomographic imaging it is advantageous to precisely orient the milled window perpendicular to the tilt axis of the electron microscope stage, to ensure an unrestricted access to the regions of interest even at high tilt angles (Figs. 1*D* and 3*B*). Moreover, this arrangement facilitates the setup of automated acquisition, in particular the placement of preparatory states like autofocussing and tracking, which must be sufficiently separated from the acquisition/exposure position (Fig. 3*B*). For the accurate orientation of the milled window in the TEM specimen holder, the support frame-grid assembly is oriented so that the ion beam milling direction, as marked by the cut-out in the support frame, is perpendicular to the TEM tilt axis (Fig. 1*C*).

Cryoelectron Tomography of FIB-Milled Windows. Ion beam micromachining opens up windows to otherwise inaccessible structures buried deep inside cells. The method is versatile enough to select

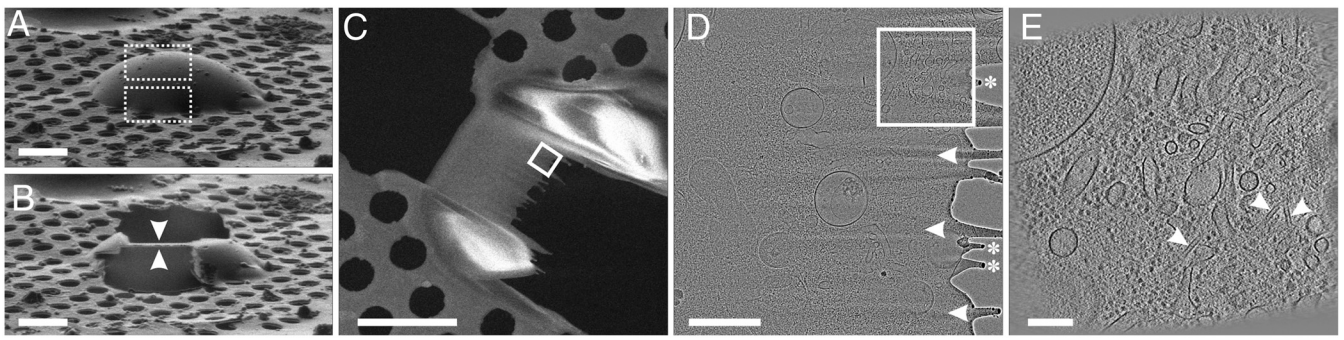

Fig. 2. FIB lamella milling of frozen-hydrated *D. discoideum*. (*A*) FIB micrograph of a frozen-hydrated cell embedded in a thin layer of ice and attached to the holey carbon support film (view in the direction of the incident ion beam). In order to prepare an in situ lamella, an upper and lower pattern for site-specific milling is defined (white dotted rectangles). (*B*) Corresponding region after FIB milling yielding the lamella (white arrowheads) which is supported on the sides by the remaining bulk ice material. (*C*) SEM top view of the same region showing the prepared area, having a size of approximately 25 μm^2. (*D*) TEM micrograph of the boxed region from (*C*) taken after cryotransfer of the lamella into the TEM. The high pass filtered image of the thinned region exhibits a view into the cell's cytoplasm. On the right side of the micrograph the milling edge can be recognized, containing putative gallium droplets (white asterisks) responsible for curtaining streaks (white arrowheads; showing direction of milling). (*E*) Slice from tomographic reconstruction of the boxed region in (*D*). Traversing microtubules (white arrowheads) and various interconnecting ducts and cisternae structures can be recognized. [Scale bars, (*A*–*C*) 5 μm, (*D*) 1 μm, (*E*) 200 nm.]

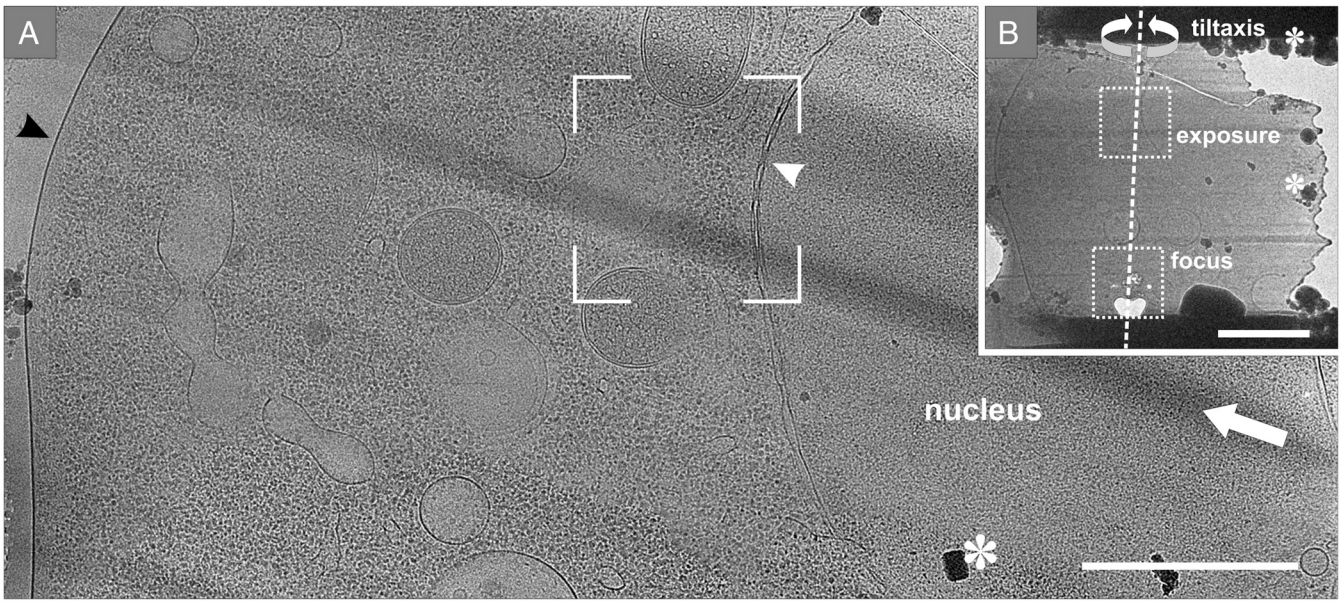

Fig. 3. Preparation of an in situ TEM lamella across a large portion of the cell's cytoplasm. (*A*) TEM micrographs stitched together to obtain an overview image of the lamella. On the left side the border region between ice and cell membrane can be recognized (black arrowhead). Within the lamella, the nuclear envelope (white arrowhead) can be clearly discerned, separating the nucleoplasm from the cytoplasm. The white arrow indicates the milling direction and highlights a prominent curtaining streak across the lamella. (*B*) Corresponding lamella imaged at lower magnification after recording of a tomographic tilt series. The dashed square regions denote the areas for tomographic exposure and focus, which are arranged along the tilt axis (for the corresponding tomographic reconstruction see Fig. 4). Some frost particles can be discerned across the lamella and on its sides (white asterisks in *A* and *B*). The framed region in (*A*) corresponds to the tomographic exposure region shown in (*B*). [Scale bars, (*A*) 1 μm, (*B*) 2 μm].

target structures under visual control (SEM or correlative cryofluorescence microscopy) and to adapt the geometry of the lamella such that the structures under scrutiny can be accommodated regardless of their 3D location within the cell. The latter is achieved by choosing appropriate target regions, milling patterns, and angle of incidence of the ion beam, as detailed in *Focused Ion Beam Milling*.

Fig. 4*A* shows a x, y-slice through a tomogram of a volume enclosing the nuclear envelope and the corresponding surface rendering (Fig. 4*D*). In the nuclear envelope the nuclear pore complexes are clearly visible (white arrows in Fig. 4*A* and colored in blue in 4*D*). *D. discoideum* NPCs measure about 125 nm in diameter and the thickness of the lamella was approximately 300 nm in this case (Fig. 4*B*). A detailed analysis of the NPCs is given below. In the surface rendered volume (Fig. 4*D*) mitochondria, parts of the endoplasmic reticulum, microtubules, and numerous ribosomes are visible. A tomogram of a second volume, 200 nm in thickness and located deep inside the cytoplasm is shown in Fig. 4 *E*–*H*.

While there is no evidence of damage caused by the ion beam, occasionally, small islets of deposited gallium can be found at the front end of the milled windows (see e.g., Fig. 2*D* and 3*B*). Most likely these islets result from differential milling of the heterogeneous cellular material which is also the main cause for mild 'curtaining' effects as visible in Fig. 3*B*. The resulting small variations in the thickness do not pose any problems in tomographic studies. There are no visible indications for artefacts resulting from gallium ion implantation; nevertheless such an implantation must be expected, but is estimated to affect only a surface layer of 10 to 20 nm which can easily be discarded from the reconstructed volume.

Structural Studies of Nuclear Pore Complexes In Situ. At present, cryoelectron tomography of organelles is routinely performed with isolated samples. In doing so, the functional context of organelles is altered, and there is always the risk that this entails structural changes. Tomograms obtained from lamellae provide insights into the structure of organelles and macromolecules in the context of the cell. One example is the nuclear pore complex, one of the largest macromolecular complexes in the cell (60–120 MDa) that acts as a gatekeeper between the nucleus and the cytoplasm. The NPC perforates the nuclear envelope, the two concentric membranes that surround the nucleus, and controls the import and export of molecules with high selectivity. Because the NPC spans two membranes and has extended structures protruding into the cytoplasm and nucleoplasm, it is difficult to assess whether the biochemical isolation of NPCs preserves their structural integrity. Tomography performed with isolated nuclei has revealed the best structure of the NPC to date (15). The advent of cryoFIB micromachining enables us now to investigate the structure of the NPC in its unperturbed cellular context.

The tomogram in Fig. 4*A* captured a portion of a nucleus and its surrounding cytoplasm in a *D. discoideum* cell. The tomogram includes 0.6 μm^2 of nuclear envelope, containing ten nuclear pores (Fig. 5*A*). Of these, three pores are fully comprised in the tomogram, while the other seven have parts that were milled away during the preparation of the lamella, or are very close to the milled surfaces of the lamella. We extracted all nuclear pores, aligned and averaged those corresponding to full NPCs using constrained correlation (16). From the subtomograms, it is evident that the NPC has eightfold symmetry (Fig. S3*A*). Of the 80 protomers in ten NPCs, we aligned and averaged 67 intact protomers, yielding the structure depicted in Fig. 5 *D*–*F*, with a resolution of 7.9 nm [Fourier shell correlation (FSC) 0.5; Fig. S3*B*]; cf. 6-nm resolution was obtained by averaging 4,182 protomers from isolated nuclei using the same type of analysis [FSC 0.5; (15); Fig. S4]. The dramatic difference between the use of FIB-prepared lamellae and of isolated nuclei in terms of the number of particles needed to obtain structural information is due to: (*i*) higher contrast owing to decreased thickness of the sample (300 nm in the lamella cf. 700 nm near the edge of isolated nuclei) and (*ii*) absence of heterogeneity that might arise from the manipulation of nuclei during isolation procedures. Furthermore, thin samples can be imaged at much lower defocus values, a requirement for attaining high-resolution, without compromising the ability to identify and align particles. Moreover, data obtained

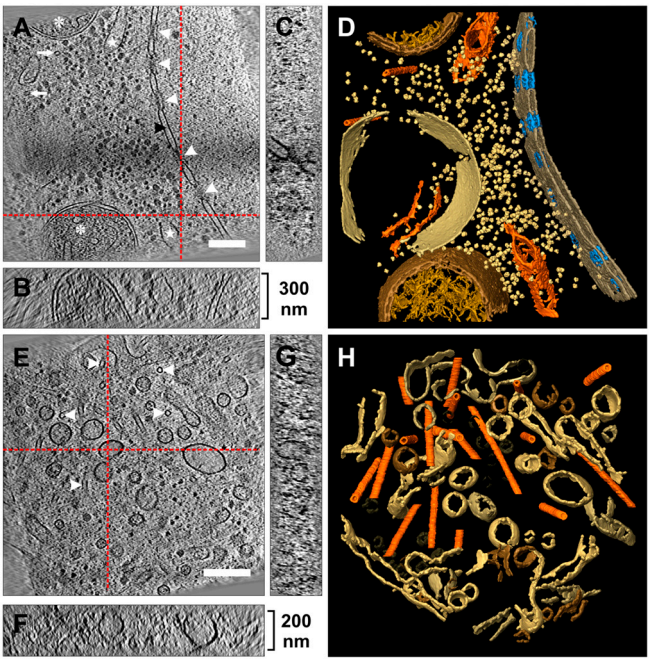

Fig. 4. Cryoelectron tomograms of *D. discoideum* cells. (*A*) Slice through the *x, y*-plane of a tomographic reconstruction (area corresponds to the exposure region described in Fig. 3) showing the nuclear envelope (black arrowhead) with nuclear pore complexes (white arrowheads) separating cytoplasm from nucleoplasm. In the cytoplasm, parts of the rough endoplasmic reticulum (white stars), tubular mitochondria (asterisks) and microtubules (white arrows) can be recognized. (*B* and *C*) Displays the corresponding *x, z* and *y, z*-planes (sectional planes are indicated by the red dashed lines). The thickness of the lamella is approximately 300 nm. (*D*) Surface rendered visualization of the tomographic volume from (*A*), displaying nuclear envelope, endoplasmic reticulum, mitochondria, microtubules, vacuolar compartment, and putative ribosomes. (*E*) Tomographic slice along the *x, y*-plane showing a cytoplasmic volume traversed by several microtubules (white arrowheads). (*F* and *G*) Corresponding *x, z* and *y, z*-planes. The overall volume has a thickness of approximately 200 nm. (*H*) Surface rendered visualization of the tomographic volume from (*E*), showing microtubules (orange) traversing the volume in various directions. A dense network of interconnecting tubular structures and vesicles can be seen. [Scale bars, (*A* and *E*) 200 nm.]

from thin samples can be corrected for the contrast transfer function directly from the data, something impossible with thick samples.

Even with the very limited dataset used in this analysis, we can draw some relevant conclusions regarding the NPC structure. First, the structure of the cytoplasmic ring, the part of the nuclear pore that extends into the cytoplasm (Fig. 5 *D–F*), looks remarkably similar to that obtained from isolated nuclei (15, 17), suggesting that in the latter case, no structural damage resulted from isolation and sample preparation of nuclei outside the cell. Further data and analysis of the NPC in situ will provide insights into the structural dynamics of the cytoplasmic filaments and the nuclear basket, which are not evident from the presented data. Second, the relative orientation and translation of the aligned protomers can be used to investigate the deviations of individual NPCs from perfect eightfold symmetry in situ. Fig. 5*B* shows that the three complete NPCs display variations in their diameter, most likely related to different states of cargo transport.

The NPCs from the tomogram shown in Fig. 4*A* exhibit anisotropic orientations, i.e., only side views. Because of the eightfold symmetry, a large portion of angular space is covered, but a missing cone in Fourier space remains. However, tomograms with different views of the nuclear envelope can be obtained by the FIB preparation technique, and the data from these tomograms can be merged to yield a nearly isotropic resolution. In some instances, particles can directly exhibit orientation isotropy even

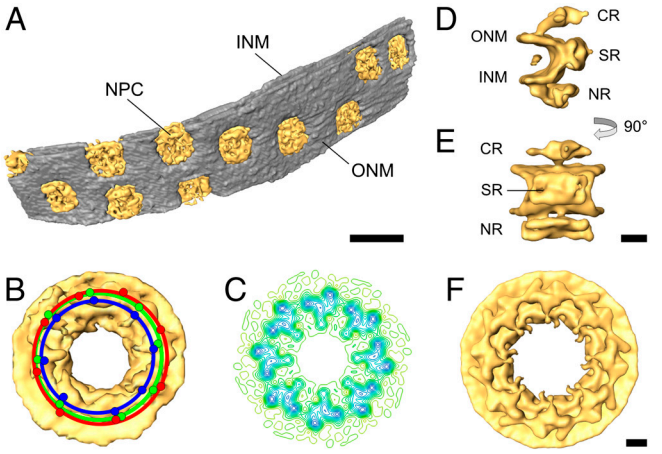

Fig. 5. Structure of the nuclear pore complex from *D. discoideum* obtained by subtomogram averaging of the NPCs from the tomogram depicted in Fig. 4. (*A*) Surface representation of the segmented nuclear envelope (NPCs: yellow; nuclear envelope: gray). (*B*) Structure of the NPC obtained by averaging the three full pores in the tomogram, without imposing rotational symmetry. The red, green, and blue dots represent the positions of the protomers for each of the pores. Note that while all pores are round, there is a variation in their diameter (10%) and from the ideal 45 degrees dictated by eightfold symmetry. (*C*) Contour-line representation of a slice of the cytoplasmic ring of the NPC. (*D* and *E*) Views of a protomer of the NPC obtained from averaging all protomers in the pores depicted in (*A*) (*D*: side view; *E*: view from the central channel). (*F*) Structure of the NPC reconstructed by applying eightfold symmetry to the protomer depicted in (*D* and *E*). For clarity, the material in the central channel (approximately 50 nm) is omitted in (*B* to *F*). (*B, C, F*) view from the cytoplasm. NPC: nuclear pore complex; ONM: outer nuclear membrane; INM: inner nuclear membrane; CR: cytoplasmic ring; SR: spoke ring; NR: nuclear ring. [Scale bars: (*A*) 200 nm, (*B–F*) 25 nm.]

within one tomogram. As an example, we extracted ribosomes from the tomogram shown in Fig. S5 and obtained structures for both membrane-bound and cytoplasmic ribosomes.

Relative Abundance of Specific Macromolecular Complexes. Cryoelectron tomography can be developed into a tool for investigating molecular crowding within cells, because the optical density obtained is proportional to the mass thickness of the material imaged. The crowding of macromolecules, is known to have profound quantitative effects on macromolecular interactions in living systems (18, 19). Hence, the in situ preparation of arbitrary cell volumes in their native hydrated state opens interesting possibilities for the study of molecular inhabitants of particular intracellular neighborhoods. As an example, a comparison of the electron optical densities between different cellular compartments visible in Fig. 4*A*, which can be interpreted as variations in mass density, is indication of a denser (12–19%) cytoplasm than nucleoplasm.

We have analyzed the spatial distribution of specific macromolecular complexes in an approximately 200 nm thick tomographic volume, which was prepared by FIB milling (Fig. S5). A *x, y*-slice through the tomogram showed the dense packing of macromolecules in the cytoplasm (Fig. S5*A*). Most prominent are electron-dense 'globular' particles, which are evenly distributed throughout the imaged cytoplasm. In order to identify these macromolecular complexes, we used a combination of subtomogram averaging and classification. A corresponding surface rendering was then used to visualize and quantify the spatial distribution of membrane-bound ribosomes (inset in Fig. S5*A*), cytoplasmic ribosomes and putative storage vesicles (Fig. S5*B*).

Discussion

FIB micromachining of frozen-hydrated cells grown directly on EM grids allows to prepare self-supporting lamellae, suitable for TEM studies. These lamellae or 'windows' can extend over areas as large as tens of square micrometers and are uniform

in thickness. In contrast to thin sections prepared by cryoultramicrotomy, the lamellae are perfectly flat with no evidence of mechanical imperfections, such as compressions or crevasses. For attaining the best possible resolution the thickness should not exceed the mean free path for inelastically scattered electrons which is approximately 200 to 400 nm in vitrified ice, depending on the operating EM voltage. On the other hand, the thickness might be dictated by the dimensions of the structure of interest, which should be accommodated with a lamella. The technology described in this communication is flexible enough to find the best compromise.

With the use of dual beam (FIB/SEM) instruments target volumes can be chosen very conveniently by operating the instrument in the SEM mode. For targeting specific supramolecular structures present in low copy numbers visual guidance by the SEM image is not sufficient. Here it would be advantageous to identify and locate regions of interest by cryofluorescence microscopy and use their coordinates for guiding the micromachining process. This strategy is used with great success in correlative cryofluorescence light microscopy and electron tomography (20, 21). However, current implementations lack resolution to precisely target subcellular features in 3D and thus, advanced optical techniques; e.g., confocal microscopy, need to be integrated into the workflow, either in the form of integrated solutions (e.g., optical microscopy integrated into the EM), or in easier to implement modular approaches.

With unstained frozen-hydrated samples of uniform thickness, such as the lamella obtained by FIB micromachining, contrast is proportional to the density of the molecular inhabitants in a given volume. In Fig. 3*A* it is apparent that the density of the mitochondria is significantly higher than that of the surrounding cytosol or of other membrane-bound organelles, which in turn, is higher than that of the nucleoplasm. The integration over the density of a given organelle or some other cellular territory provides a relative measure for the local mass density; i.e., molecular crowding. This analysis opens up new opportunities for quantitative measurements of crowding in subcellular compartments or territories once suitable methods for calibration have been developed.

Hitherto visual proteomics (22, 23) based on the identification and localization of macromolecules by pattern recognition methods, such as template matching (24, 25), was restricted to small prokaryotic cells or very thin regions of eukaryotic cells. The windows prepared by FIB micromachining make it possible now to extend such studies to all cells that can be grown or deposited on EM specimen supports. The localization of macromolecules in tomograms followed by subtomogram averaging and classification offers opportunities for in situ structural studies. Having control over the thickness of the sample studied by tomography allows to push resolution to the limits.

Methods

Preparation and Vitrification of Cells. *Dictyostelium discoideum* strain AX2-214 (wild type) cells were cultivated at 23 ± 2 °C in polystyrene cell culture dishes containing nutrient medium with maltose and harvested before they had reached confluency (26). Cells were washed twice in 17 mM K/Na-phosphate buffer, pH 6.0 (PB) before they were incubated in PB and allowed to settle on holey carbon coated 200 mesh gold EM grids (Quantifoil and Protochips). Grids were removed from culture dishes and excess PB was removed by blotting from the reverse side and grids were plunge-frozen by rapid immersion in liquid ethane (27) using a custom-built vitrification device.

Mounting of EM Grids into a Supporting Frame Structure for Cryogenic Transfers. In order to protect the delicate gold EM grids from mechanical distortions damaging the thin ice layers during the transfer steps, we mounted them after vitrification on a custom-modified supporting frame structure (Fig. S1), referred to as the autogrid (AutoGrid™ sample holder, FEI). The autogrid holder was modified by a cut-out within the frame structure (Fig. 1 *B* and *C*; Fig. S1*B*) to permit accessibility for shallow incident ion beams in the FIB microscope (Quanta 3D FEG, FEI).

In order to protect the vitrified specimen from frost contamination caused by ambient humidity and to ensure maximal thermal stability, we used a cryoshuttle together with a loading station as previously described (12). Both parts were adapted to a Polarprep 2000T cryosystem (Quorum) mounted on the FIB instrument. The cryoshuttle was modified to accommodate two autogrids containing vitrified EM samples.

Focused Ion Beam Milling. Using autogrids, the loading station and the transfer shuttle, frozen-hydrated EM samples were ablated with a dual-beam (FIB/SEM) instrument (Quanta 3D FEG, FEI) equipped with a custom-built 360° rotatable cryostage (28) operated at −160 °C and adapted to a cryoSEM preparation system (PP2000T, Quorum). The vitrified samples were imaged at 5–10 keV with the SEM and milled with 30 keV gallium ions by scanning the regions of interest at shallow tilt angles using a beam current of 30–50 pA unless indicated otherwise.

For preparation of self-supporting lamellae, target cells were identified by imaging secondary electrons, generated by the electron beam (Selection can also involve an additional step, namely, cryofluorescence microscopy). By using cryostage tilt and rotation, a target cell was properly oriented for ion beam milling, in order to fulfill the geometrical requirements for a glancing angle of incidence. Before defining patterns for milling an overview image was taken by imaging secondary electrons generated by the Ga^+ beam. In a first step, for coarse milling, this overview image is used to place an upper and lower rectangular milling pattern across the designated target cell, flanking the intended area for lamella preparation and leaving an area of 1–2 μm in between these patterns. The width of the milling patterns is governed by the respective cell dimensions. Typically, a pattern should not cover more than two thirds of the cell's visible width, in order to provide enough lateral support for the lamella. The height of each pattern must cover the entire visible cellular area. Frozen-hydrated material was then removed by scanning the selected regions in a parallel mode with a rapidly rastering Ga^+ beam using a current of 300 pA. The higher currents used during coarse milling, allow for a faster removal of bulk frozen-hydrated material. In a second step, fine milling was carried out by placing and redefining the rectangular patterns closer to each other, leaving 300–600 nm between them—the intended final thickness of the lamella. In order to minimize potential ion beam damage effects, the milling current was lowered to 30–50 pA and milling at these positions was carried out in a parallel mode by rapidly rastering with a 30 keV Ga^+ beam. Depending on the size of cells being selected, coarse milling typically takes 10 min, whereas fine milling requires roughly twice that time. We selected cells for milling that were located within the central region of a mesh (to prevent obstruction of the electron beam by the grid bars during tomography) and in meshes close to the center of the EM grid (to ensure TEM stage accessibility). We typically selected one area/cell per mesh for milling. Taking into account milling times and sample characteristics, the yield per grid was in the range of 6–8 milled regions. The reproducibility of the lamella milling was excellent from grid to grid and the rate of successfully transferred lamellae into the TEM was above 90%.

Cryoelectron Microscopy and Tomography. Tilt series typically covering an angular range from −60° to 60° with 1.5° or 2° tilt increments were recorded automatically (29, 30) under low-dose conditions using a Tecnai G2 Polara microscope (FEI) equipped with a GIF 2002 postcolumn energy filter and slow-scan CCD camera with $2,048 \times 2,048$ pixels (Gatan). The TEM was operated at an accelerating voltage of 300 kV; the pixel size in the object-plane was between 0.46 nm and 0.71 nm. Images were recorded with defocus values ranging from −6 to −8 μm. The projection images were aligned using cross-correlation procedures and reconstructed by a weighted back-projection algorithm as implemented in the EM and TOM software packages (31, 32). Visualization and surface rendering was performed using the Amira software (33). Images were stitched together and adjusted for matching contrast and brightness using Adobe Photoshop CS4.

Subtomogram Averaging and Classification. For the structure of the NPC, we picked the particles by visual inspection. The initial orientation of the NPCs was obtained by fitting an ellipsoid to the nuclear envelope, so that the *z*-axis pointed into the cytoplasm and perpendicular to the membrane. We first averaged the three full NPCs and determined the eightfold symmetry using averaged rotational correlation (Fig. S3). In order to improve the resolution of the reconstruction and to assess the variability in the structure of the pores in situ, we considered each of the eight protomers of the NPC as an individual particle. We then extracted subtomograms for each of these particles that contained the protomer plus half of each of the two neighboring protomers (corresponding to a fourth of the NPC). Constrained-correlation alignment

of the 24 protomers from the three full pores, plus 43 protomers from the partial pores yielded the structure shown in Fig. 5 *D* and *E*.

For identification of macromolecular complexes in cryoelectron tomograms covering cytoplasmic regions, we used a combination of subtomogram averaging and classification. In a first step, the cross correlation function between two times binned tomograms and a 25 nm spherical template was computed. From the corresponding correlation peaks subvolumes ($24 \times 24 \times 24$ voxels) were extracted and classified into 12 classes via a missing-wedge corrected multi reference classification procedure, using the initial template with different representations of Gaussian noise added as starting references. Particles converged into four evident classes, representing membrane-bound ribosomes, cytoplasmic ribosomes, putative storage vesicles, and vacuolar ATPases. Next, classified particles were reconstructed using a binning of one. For subsequent subtomogram averaging (16) the same spherical template was used as an initial reference. During subtomogram alignment, particles with correlation values below 0.3 were discarded from further analysis. The resolution of the averaged membrane-bound and cytoplasmic ribosomes was assessed based on the FSC, yielding approximately 6.1 nm for membrane-bound and approximately 5 nm for cytoplasmic ribosomes at the 0.5 threshold criterion.

ACKNOWLEDGMENTS. We thank Lena Fitting-Kourkoutis for fruitful discussions, Guenther Gerisch and Mary Ecke for providing AX2 cells and the members of the fine mechanical workshop of the Department of Structural Biology for the construction of all essential components. The research leading to these results has received funding from the European Commission's 7th Framework Programme (grant agreement HEALTH-F4-2008-201648/PROSPECTS, and a Marie Curie fellowship to E.V.), from the Federal Ministry of Education and Research (BMBF) and from an inter-institutional research initiative of the Max Planck Society.

1. Koster AJ, et al. (1997) Perspectives of molecular and cellular electron tomography. *J Struct Biol* 120:276–308.
2. Lucic V, Forster F, Baumeister W (2005) Structural studies by electron tomography: from cells to molecules. *Annu Rev Biochem* 74:833–865.
3. Baumeister W (2005) From proteomic inventory to architecture. *FEBS Lett* 579:933–937.
4. Grunewald K, et al. (2003) Three-dimensional structure of herpes simplex virus from cryo-electron tomography. *Science* 302:1396–1398.
5. Medalia O, et al. (2002) Macromolecular architecture in eukaryotic cells visualized by cryoelectron tomography. *Science* 298:1209–1213.
6. Nicastro D, et al. (2006) The molecular architecture of axonemes revealed by cryoelectron tomography. *Science* 313:944–948.
7. Brandt F, Carlson LA, Hartl FU, Baumeister W, Grunewald K (2010) The three-dimensional organization of polyribosomes in intact human cells. *Mol Cell* 39:560–569.
8. Al-Amoudi A, Studer D, Dubochet J (2005) Cutting artefacts and cutting process in vitreous sections for cryo-electron microscopy. *J Struct Biol* 150:109–121.
9. Hsieh CE, Leith A, Mannella CA, Frank J, Marko M (2006) Towards high-resolution three-dimensional imaging of native mammalian tissue: electron tomography of frozen-hydrated rat liver sections. *J Struct Biol* 153:1–13.
10. McDowall AW, et al. (1983) Electron microscopy of frozen hydrated sections of vitreous ice and vitrified biological samples. *J Microsc* 131:1–9.
11. Marko M, Hsieh C, Schalek R, Frank J, Mannella C (2007) Focused-ion-beam thinning of frozen-hydrated biological specimens for cryo-electron microscopy. *Nat Methods* 4:215–217.
12. Rigort A, et al. (2010) Micromachining tools and correlative approaches for cellular cryo-electron tomography. *J Struct Biol* 172:169–179.
13. Hayles MF, et al. (2010) The making of frozen-hydrated, vitreous lamellas from cells for cryo-electron microscopy. *J Struct Biol* 172:180–190.
14. Overwijk MHF, Vandenheuvel FC, Bullelieuwma CWT (1993) Novel scheme for the preparation of transmission electron-microscopy specimens with a focused ion-beam. *J Vac Sci Technol B* 11:2021–2024.
15. Beck M, Lucic V, Forster F, Baumeister W, Medalia O (2007) Snapshots of nuclear pore complexes in action captured by cryo-electron tomography. *Nature* 449:611–615.
16. Forster F, Medalia O, Zauberman N, Baumeister W, Fass D (2005) Retrovirus envelope protein complex structure in situ studied by cryo-electron tomography. *Proc Natl Acad Sci USA* 102:4729–4734.
17. Beck M, et al. (2004) Nuclear pore complex structure and dynamics revealed by cryoelectron tomography. *Science* 306:1387–1390.
18. Ellis RJ (2001) Macromolecular crowding: an important but neglected aspect of the intracellular environment. *Curr Opin Struct Biol* 11:114–119.
19. Minton AP (1995) Confinement as a determinant of macromolecular structure and reactivity. II. Effects of weakly attractive interactions between confined macrosolutes and confining structures. *Biophys J* 68:1311–1322.
20. Jun S, et al. (2011) Direct visualization of HIV-1 with correlative live-cell microscopy and cryo-electron tomography. *Structure* 19:1573–1581.
21. Lucic V, et al. (2007) Multiscale imaging of neurons grown in culture: from light microscopy to cryo-electron tomography. *J Struct Biol* 160:146–156.
22. Beck M, et al. (2009) Visual proteomics of the human pathogen Leptospira interrogans. *Nat Methods* 6:817–823.
23. Nickell S, Kofler C, Leis AP, Baumeister W (2006) A visual approach to proteomics. *Nat Rev Mol Cell Biol* 7:225–230.
24. Bohm J, et al. (2000) Toward detecting and identifying macromolecules in a cellular context: template matching applied to electron tomograms. *Proc Natl Acad Sci USA* 97:14245–14250.
25. Frangakis AS, et al. (2002) Identification of macromolecular complexes in cryoelectron tomograms of phantom cells. *Proc Natl Acad Sci USA* 99:14153–14158.
26. Watts DJ, Ashworth JM (1970) Growth of myxamoebae of cellular slime mould dictyostelium-discoideum in axenic culture. *Biochem J* 119:171–174.
27. Dubochet J, Mcdowall AW (1981) Vitrification of pure water for electron-microscopy. *J Microsc-Oxford* 124:Rp3–Rp4.
28. Rigort A, et al. (2010) A 360° rotatable cryo-FIB stage for micromachining frozen-hydrated specimens for cryo-electron tomography. *Microsc Microanal* 16(Suppl. 2): 220–221.
29. Grimm R, et al. (1997) Energy filtered electron tomography of ice-embedded actin and vesicles. *Biophysical J* 72:482–489.
30. Korinek A, Beck F, Baumeister W, Nickell S, Plitzko JM (2011) Computer controlled cryo-electron microscopy—TOM(2) a software package for high-throughput applications. *J Struct Biol* 175:394–405.
31. Hegerl R (1996) The EM program package: a platform for image processing in biological electron microscopy. *J Struct Biol* 116:30–34.
32. Nickell S, et al. (2005) TOM software toolbox: acquisition and analysis for electron tomography. *J Struct Biol* 149:227–234.
33. Stalling D, Westerhoff M, Hege H-C (2005) Amira: A Highly Interactive System for Visual Data Analysis. *Visualization Handbook*, eds DH Charles and RJ Chris (Butterworth-Heinemann, Burlington), pp 749–767.